Chin. Phys. Lett. **39**, 030302 (2022) **Express Letter**

# Realization of Fast All-Microwave Controlled-Z Gates with a Tunable Coupler

Shaowei Li(李少炜)[1,2,3], Daojin Fan(范道金)[1,2,3], Ming Gong(龚明)[1,2,3], Yangsen Ye(叶杨森)[1,2,3], Xiawei Chen(陈厦微)[1,2,3], Yulin Wu(吴玉林)[1,2,3], Huijie Guan(关卉杰)[1,2,3], Hui Deng(邓辉)[1,2,3], Hao Rong(荣皓)[1,2,3], He-Liang Huang(黄合良)[1,2,3], Chen Zha(查辰)[1,2,3], Kai Yan(严凯)[1,2,3], Shaojun Guo(郭少俊)[1,2,3], Haoran Qian(钱浩然)[1,2,3], Haibin Zhang(张海斌)[1,2,3], Fusheng Chen(陈福升)[1,2,3], Qingling Zhu(朱庆玲)[1,2,3], Youwei Zhao(赵有为)[1,2,3], Shiyu Wang(王石宇)[1,2,3], Chong Ying(应翀)[1,2,3], Sirui Cao(曹思睿)[1,2,3], Jiale Yu(余家乐)[1,2,3], Futian Liang(梁福田)[1,2,3], Yu Xu(徐昱)[1,2,3], Jin Lin(林金)[1,2,3], Cheng Guo(郭成)[1,2,3], Lihua Sun(孙丽华)[1,2,3], Na Li(李娜)[1,2,3], Lianchen Han(韩廉琛)[1,2,3], Cheng-Zhi Peng(彭承志)[1,2,3], Xiaobo Zhu(朱晓波)[1,2,3*], and Jian-Wei Pan(潘建伟)[1,2,3]

[1]*Department of Modern Physics, University of Science and Technology of China, Hefei 230026, China*
[2]*Shanghai Branch, CAS Center for Excellence in Quantum Information and Quantum Physics, University of Science and Technology of China, Shanghai 201315, China*
[3]*Shanghai Research Center for Quantum Sciences, Shanghai 201315, China*

(Received 6 January 2022; accepted 29 January 2022; published online 10 February 2022)

The development of high-fidelity two-qubit quantum gates is essential for digital quantum computing. Here, we propose and realize an all-microwave parametric controlled-Z (CZ) gates by coupling strength modulation in a superconducting Transmon qubit system with tunable couplers. After optimizing the design of the tunable coupler together with the control pulse numerically, we experimentally realized a 100 ns CZ gate with high fidelity of 99.38%±0.34% and the control error being 0.1%. We note that our CZ gates are not affected by pulse distortion and do not need pulse correction, providing a solution for the real-time pulse generation in a dynamic quantum feedback circuit. With the expectation of utilizing our all-microwave control scheme to reduce the number of control lines through frequency multiplexing in the future, our scheme draws a blueprint for the high-integrable quantum hardware design.

DOI: 10.1088/0256-307X/39/3/030302

Digital quantum gates are the basis for the construction of gate-based quantum error correction, which was proposed to realize universal quantum computing.[1,2] In practical realization, single-qubit quantum gates are usually easy to implement and have high fidelities.[3] The multi-qubit quantum gates involve the interaction of multiple qubits, thus are much more difficult to implement, and have become one of the important indicators of whether quantum error correction can be achieved.[2,4] Profited by the easy-to-control characteristics of superconducting qubits, two-qubit gates, including controlled-Z (CZ),[4−16] CNOT,[17,18] and fSim gates,[19] with fidelity reaching the threshold of error correction has already been realized.

In superconducting circuits, most of the implementation of two-qubit gates can be classified into unipolar-pulse-based and microwave-based parametric gates. Benefiting from the shorter gate time, the unipolar-pulse-based CZ gates generally achieves higher fidelity than the microwave-based pulse scheme.[4−12,14−18] However, for most of these CZ gates, a significant part of the control error in experiment comes from the time-domain correlation noise caused by the pulse distortion.[5−7,10,12] The solution includes correction of the control pulse[20,21] and net-zero control pulse design.[5] Pulse correction requires not only prior knowledge of the distortion formulation but also a large number of computing resources to generate the waveform in advance,[4,21] and is thus difficult to realize in real-time waveform generation architecture.[2,22] The other solution is to utilize the net-zero control pulse at qubits' sweet point.[5] Such scheme requires that the qubits must work at their sweet point for efficient interaction. Therefore, higher requirements are put forward for the accuracy control of qubit frequency in device fabrication. In contrast, the microwave-based two-qubit gates have been realized by applying a full microwave control pulse,[13,14,17,18] which is less affected by pulse distortion. However, those gates usually take a longer time to implement, thus encountering more decoherence.

Here, we provide a microwave-based two-qubit gates scheme implemented on a superconducting Transmon qubits architecture with tunable couplers. The CZ gate is realized by applying a net-zero mi-

*Corresponding author. Email: xbzhu16@ustc.edu.cn
© 2022 Chinese Physical Society and IOP Publishing Ltd

crowave pulse on the coupler flux. Compared with microwave-based gates like cross-resonance CNOT gate and other parametric CZ gates, we utilize a wide-range tunable coupler with the coupling strength that can be turned on to be above 10 MHz in both directions. This design significantly shortens the implementation time of microwave CZ gates. With this scheme, we achieved a 100 ns CZ gate with a fidelity of 99.38%±0.34%, where the confidence interval is 95%. Meanwhile, as the coupler has a coupling off point, we can set the coupler flux for idle and single-qubit gates at the decoupling point. As the qubits are decoupled during idle and single-qubit gates, it is not necessary to consider the effect of residual coupling to detune the frequencies of any qubits far away. Therefore, as the single-qubit gate and CZ gate do not contain any unipolar pulse, there is no need to consider pulse correction. We also found that when the frequency of microwaves deviates from the optimal frequency by 5–10 MHz, the target quantum state will no longer have a significant evolution. Therefore, we believe that this two-qubit-gate scheme has the potential for frequency multiplexing in the future, especially in combination with suitable on-chip filter designs.

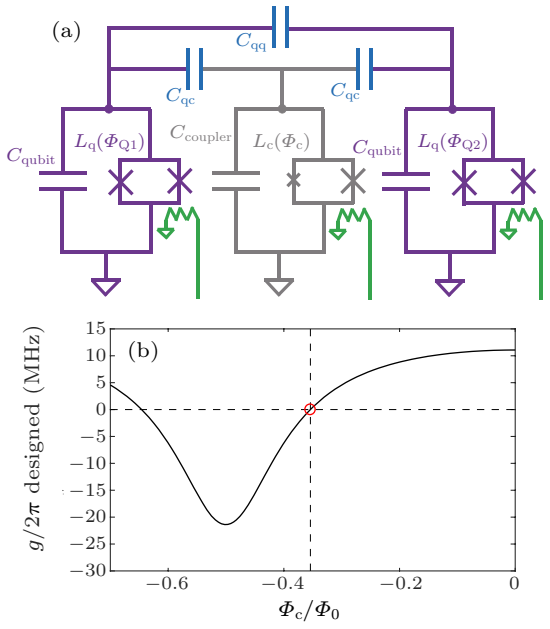


**Fig. 1.** (a) Schematic diagram of qubit and coupler circuits. Purple is the qubit, gray is the coupler, blue is the coupling capacitor, and green is the control line. (b) The theoretical design of coupling strength. The capacitive coupler is designed with an asymmetrical junction, and the red circle is the coupling zero point.

The circuit diagram of our quantum coupler qubit design is shown in Fig. 1(a). Due to the insufficient precision of the Josephson junction performance prepared in the experiment, we need to fine-tune the qubit frequency according to the decoherence performance and frequency collision. Therefore, our qubit is designed to be frequency tunable with a flux control line, and we can also realize a single-qubit gate by this control line. To reduce the influence of residual XX coupling and improve the performance of parallel single-qubit gates, our coupler is designed to contain an XX coupling-off point. We set the flux of the coupler near this XX coupling-off point when applying single-qubit gates.

We designed our coupler parameters based on our simulation results (see the Supplementary Information), specifically $C_{\rm qubit} = 70.9\,{\rm fF}$, $C_{\rm coupler} = 80.3\,{\rm fF}$, $C_{\rm qq} = 0.71\,{\rm fF}$, $C_{\rm qc} = 13.6\,{\rm fF}$. The coupler we designed can achieve a coupling strength above 10 MHz in both directions to make it efficient to implement a high-fidelity CZ gate. Since the flux pulse is symmetrical during implementing CZ, we design the coupler loop as asymmetric Josephson junctions to avoid the coupler frequency being too close to the qubit frequency. For our design parameters, the coupling strength has a minimum value at $\Phi_{\rm c}/\Phi_0 = 0.5$, measured to be $-22\,{\rm MHz}$, and the frequency difference between the qubit and coupler is larger than 2 GHz.

According to experimental data, we fit the Josephson junction parameters of our qubits and coupler. The $I_{\rm c}$ of qubits are fitted to be 14.0 nA and 14.0 nA and the $I_{\rm c}$ of coupler are fitted to be 35.0 nA and 70.4 nA. The coupling strength between the two qubits varies from $-22\,{\rm MHz}$ to 11 MHz [see Fig. 1(b)]. To trade off the influence of the residual XX coupling and ZZ coupling, we choose the idle working point near the $g_{\rm xx} = 0$, where $\Phi_{\rm c}/\Phi_0 = -0.35$ [red circle in Fig. 1(b)].

In the coupling strength tunable transmon qubit, if we ignore the dress state caused by the interaction between the qubit and coupler, the interaction subspace Hamiltonian of two qubits can be simplified as

$$\begin{aligned}\hat{H}_{\rm sub}(t) =& \hbar\omega_{10}|10\rangle\langle 10| + \hbar\omega_{01}|01\rangle\langle 01| + \hbar\omega_{11}|11\rangle\langle 11| \\ &+ \hbar\omega_{02}|02\rangle\langle 02| + \hbar\omega_{20}|20\rangle\langle 20| \\ &+ \hbar g(t)(|10\rangle\langle 01| + |01\rangle\langle 10|) \\ &+ \sqrt{2}\hbar g(t)(|02\rangle\langle 11| + |11\rangle\langle 02|) \\ &+ \sqrt{2}\hbar g(t)(|20\rangle\langle 11| + |11\rangle\langle 20|). \end{aligned} \tag{1}$$

We assume the difference of qubit frequency as $\Delta = \omega_{10} - \omega_{01} > 0$, and coupling strength as $g(t) = \Omega(t)\cos(\omega_{\rm target}t + \phi)$. If $\omega$ satisfies $\omega_{\rm target} = |\omega_{11} - \omega_{20}|$, the $|11\rangle$ and $|20\rangle$ will interact in resonance, as shown by the black line in Fig. 2(a). Here $\Omega(t)$ is the envelope function and $\omega_{\rm target}$ is the driven frequency. To set a reasonable working point, it must satisfy that $|\Delta_{\rm leak} - \omega_{\rm target}| \gg \Omega(t)$ and $|\Delta - \omega_{\rm target}| \gg \Omega(t)$ to avoid the other two interactions, as shown by the thin red line in Fig. 2(a), where $\Delta_{\rm leak} = |\omega_{11} - \omega_{02}|$.

However, the above Hamiltonian is only an approximate demonstration. For the actual tunable coupling qubits, one needs to be cautious about the following two points. First, the energy eigenstate is a dressed state, and $\omega_{01}$ changes with coupler flux. The qubit

center frequency will have a shift of 0–5 MHz according to the driving amplitude $\Omega(t)$, which will impact the decoherence performance of the qubit. Second, the relationship between coupling strength and coupler flux is nonlinear. To generate a net-zero microwave pulse, the variation in flux is sinusoidal-like [see red line in Fig. 2(b)], and the symmetrical flux variation will produce asymmetrical coupling strength variation [see black line in Fig. 2(b)]. This means that a monochromatic flux pulse will result in a coupling strength pulse with multiple peaks in the frequency domain [see Fig. 2(c)]. Therefore, we should also consider the influence of these frequency components when selecting the qubit working point [see Fig. 2(d)]. We checked the gate error of the CZ gate that can be achieved under different frequency settings $\Delta$ after 200 iterations of Nelder Mead algorithm.[23–25] We found that if the unwanted resonance interactions induced by the $\omega_{\text{target}}$ and $2\omega_{\text{target}}$ are avoided, a CZ gate with fidelity higher than 99.99% can be easily achieved.

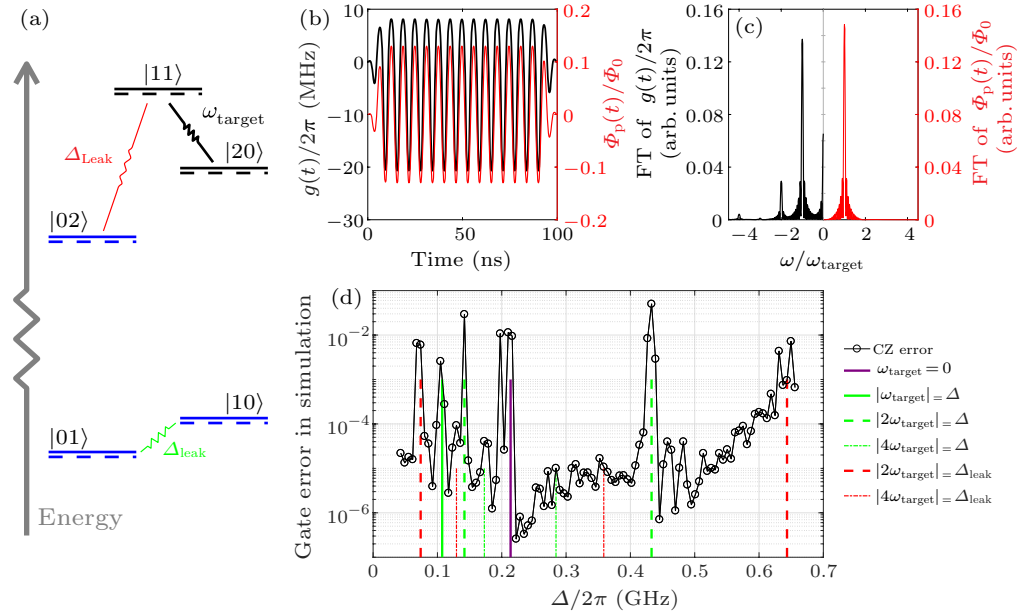


**Fig. 2.** (a) Equivalent energy level when microwave pulse is applied to the coupler loop. The solid lines represent the energies at idle time, and the dashed lines represent the energies shift during the input microwave. There are three interactions involved: between $|01\rangle$, $|10\rangle$, between $|11\rangle$, $|02\rangle$, and between $|11\rangle$, $|20\rangle$. (b) The flux in the coupler and the coupling strength between two qubits during the microwave pulse. The relationship between the flux variation and time is a sinusoidal pulse (red solid line), $\Phi_{\text{p}}(t) = A(t)\cos(\omega_{\text{input}}t + \phi)$, where $\Phi_{\text{p}}(t)$ is the extra flux superimposed on coupler, and $A(t)$ is the envelope of the microwave. The positive and negative coupling is asymmetrical because of the nonlinear relationship between the flux variation and the coupling strength (solid black line). (c) The Fourier component of flux and coupling strength in (b). The main frequency component of flux is at $\omega_{\text{input}}$, shown on the right side. From the left side, we can see the frequency components are significantly placed at 0, $\omega_{\text{input}}$, $2\omega_{\text{input}}$, $3\omega_{\text{input}}$, $4\omega_{\text{input}}$ and even other higher frequency components. (d) Gate error in simulation. The CZ error after 200 iterations for the envelope and coupler design we used (see the Supplementary Information). The vertical lines of different colors indicate that the resonance interaction between $\Delta$ and $\Delta_{\text{leak}}$ has been induced, and a large error has been caused.

**Table 1.** Qubit performances at selected working points.

| Qubit | $f_{01,\text{max}}$ | $f_{01,\text{idle}}$ | Anharmonicity | $T_{1,\text{idle}}$ | $T_{1,\text{CZ}}$ | $T^*_{2,\text{idle}}$ |
|---|---|---|---|---|---|---|
| Q1 | 4.770 GHz | 4.770 GHz | −232 MHz | 32.2 μs | 36.0 μs | 13.5 μs |
| Q2 | 4.847 GHz | 4.839 GHz | −230 MHz | 58.5 μs | 45.6 μs | 13.3 μs |

The two qubits we used to perform the experiment are named Q1 and Q2. Considering the decoherent performance and avoiding unwanted resonance interactions, we set the qubit idle point shown in Table 1. The performances in Table 1 are measured at $\Phi_{\text{c}}/\Phi_0 = -0.35$, and $T_{1,\text{CZ}}$ is obtained by averaging the frequency from 0 to 5 MHz below the idle point.

We set the microwave active time to 250 ns and select a suitable envelope $A(t)$ to measure the population exchange between $|11\rangle$ and $|20\rangle$ and the control phase under different microwave amplitudes. Figure 3(a) depicts the circuit for measuring transition rate from and back to $|11\rangle$ state and Fig. 3(c) describes this quantity as a function of microwave amplitude $A(t)$ and frequency. Figure 3(b) shows the circuit for measuring relative phase between $|0\rangle$ and $|1\rangle$ state with Q2 being either $|0\rangle$ or $|1\rangle$. The difference between the two outcomes relates to the control phase

[see Fig. 4(d)]. We found that when the microwave amplitude is near 0.06, and the microwave frequency is near the resonance frequency, the population of $|11\rangle$ in the final state approaches 1, and the control phase is close to $\pi$, which implies a reliable CZ gate. Such results serve as a rough estimation of the parameters of a CZ gate, from which we will fine-tune each value by considering more realistic situations.

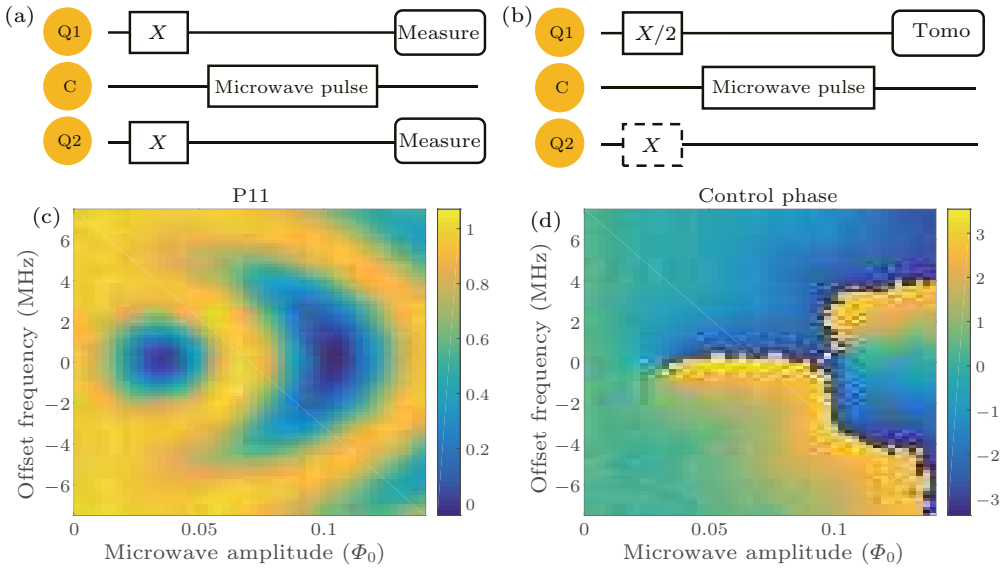


**Fig. 3.** (a) Quantum sequence for detecting the swap between $|11\rangle$ and $|20\rangle$. We prepare two qubits in $|11\rangle$ by two X gates for each qubit, then apply microwave pulse at coupler control line and measure the final population of $|11\rangle$. (b) Quantum sequence for detecting the control phase. We prepare Q1 in a superposition state and measure the phase $\theta_1$ and $\theta_2$ of Q1 after microwave pulse by applying X gate to Q2 or not. We calculate the control phase according to the formula $\theta_{\text{control}} = \theta_1 - \theta_2$. (c) The result is measured in the experiment by the sequence in (a). The $x$-axis is the averaging amplitude $\bar{A}(t)$ of the microwave pulse during the active time, and the $y$-axis is the deviation of the microwave pulse frequency from the resonance frequency. (d) The result is measured in the experiment by the sequence in (b). The control phase is measured by Q1.

The error of the CZ gate in the experiment mainly includes the following four types: decoherence error, leakage error caused by residue population in $|20\rangle$ and $|02\rangle$, phase error caused by inaccurate control phase, and swap error caused by interaction between $|01\rangle$ and $|10\rangle$.[26–28] To mitigate these errors, we need to optimize the envelope of the control pulse. We first parameterize the envelope as

$$A(t) = \lambda_1 \sin\frac{\pi t}{T_a} + \lambda_2\left(1 - \cos\frac{2\pi t}{T_a}\right) + \lambda_3 \sin\frac{3\pi t}{T_a} + \lambda_4\left(1 - \cos\frac{4\pi t}{T_a}\right). \quad (2)$$

Here $T_a$ is the microwave active time, and $\lambda$ is the envelope parameter that needs to be optimized. To reduce the decoherence error, we set $T_a = 100$ ns. Furthermore, we initialized the $\lambda$ ratio according to the result of the numerical simulation ($\lambda_1 : \lambda_2 : \lambda_3 : \lambda_4 = -0.0760 : 1.0000 : 0.4222 : -0.1636$), then we measured the swap probability and control phase to determine the initial value of $\bar{A}(t)$ and microwave frequency (see Fig. 3). Next, we optimized $\lambda_1$, $\lambda_3$, $\lambda_4$, $\bar{A}(t)$ and microwave frequency to improve the fidelity of the CZ gate through 50 to 100 iterations, as described in Fig. 4(a). The evaluation function related to CZ fidelity is measured by the randomized benchmarking (RB) method.[29–31] Some experimental methods can reduce the noise in the measurement of this evaluation function. Depending on the error tolerance, each measurement may take 20 to 60 s, which amounts to a total cost of about 1 to 2 h for a complete optimization, including data processing.

After 100 iterations, we obtain the optimized control microwave pulse of the CZ gate as shown in Fig. 4(b). In addition to the active time of 100 ns, we add three ns idle time before and after the active time to avoid timing misalignment and microwave residue. The average amplitude is determined by optimization, and the actual CZ pulse reaching the coupler will be smaller compared to the same input amplitude of DC bias due to attenuation and bonding-wire reflections at $\omega_{\text{target}}$.

We use cross-entropy benchmarking (XEB) and speckle purity benchmarking (SPB)[19,32,33] to quantify the error source of our single-qubit gate and CZ gate. The XEB circuits and results of single-qubit gate and CZ gate are shown in Figs. 4(c) and 4(d). We fitted the sequence fidelity and purity fidelity data according to $\alpha = Ap_{\text{xeb}}^m + B$, $\sqrt{P} = Ap_{\text{spb}}^m + B$ (the calculation formulas of $\alpha$ and $\sqrt{P}$ are described in

the Supplementary Information), and we calculated the cycle Pauli error from the formula $r_{\mathrm{p,xeb(spb)}} = (1-p_{\mathrm{xeb(spb)}})(4^N-1)/4^N$, where $N$ is the number of qubit. The Pauli error of CZ gate is extracted from formula $(1-r_{\mathrm{p,cycle}}) = (1-r_{\mathrm{p,CZ}})(1-r_{\mathrm{p},Q1})(1-r_{\mathrm{p},Q2})$. The population of leakage is fitted by formula of $\epsilon_{\mathrm{leak}} = Ap_{\mathrm{leak}}^m + B$, and we calculated leakage error such that $r_{\mathrm{leak}} = -A(1-p_{\mathrm{leak}})(4^N-1)/4^N$. We extract control Pauli error as $r_{\mathrm{p,ctrl}} = r_{\mathrm{p,xeb}} - r_{\mathrm{p,spb}}$ and decoherence Pauli error as $r_{\mathrm{p,dec}} = r_{\mathrm{p,spb}} - r_{\mathrm{leak}}$. The gate fidelity can be obtained as $F = 1-r_{\mathrm{p}}2^N/(2^N+1)$, and CZ fidelity calculated to be $99.38\% \pm 0.34\%$ with 95% confidence. The single-qubit gate and CZ gate error budget is shown in Table 2.

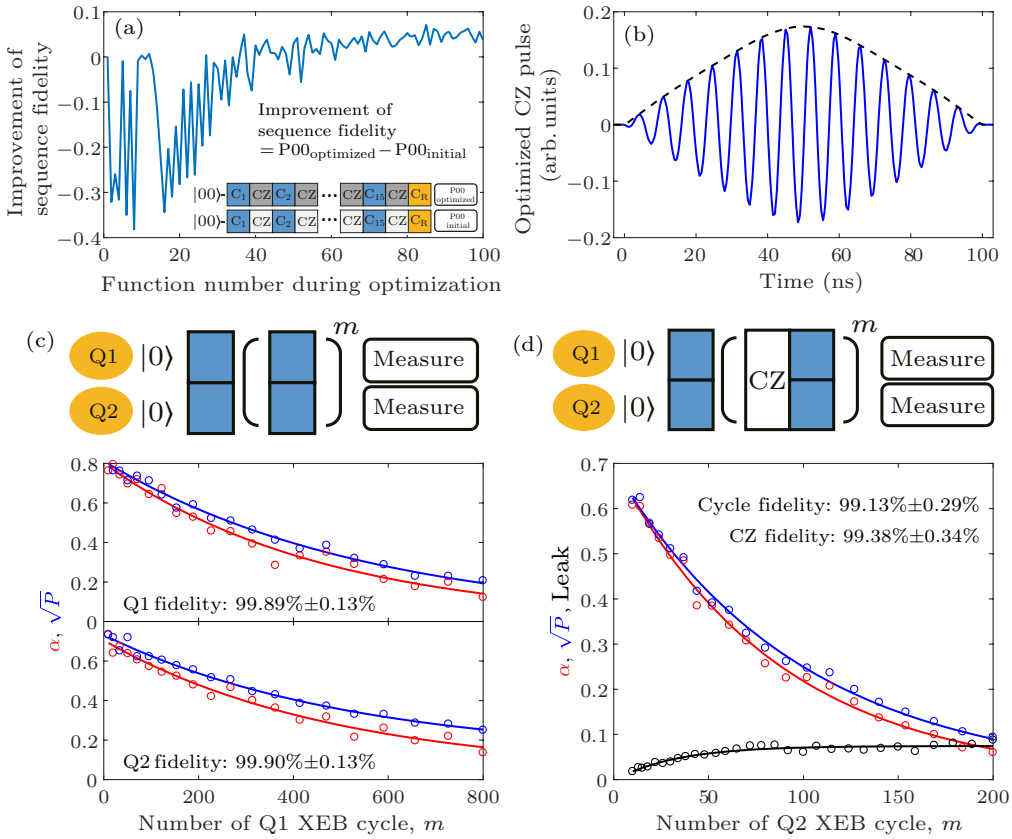


**Fig. 4.** (a) Optimization of CZ gate. The cost function is obtained by sequence fidelity of interleaved RB that contains 15 Clifford gates and an inversed gate. (b) The optimized control microwave pulse. The solid line is the applied microwave, and the dashed line is the envelope. (c) XEB and SPB results of single-qubit cycle. The sequence of the single-qubit cycle is shown in the upper part. The circle and the solid lines are experimental data and the fitting result of Q1 and Q2. Blue and red are data of $\sqrt{P}$ and $\alpha$. (d) XEB, SPB, leakage results of CZ cycle. The sequence of the CZ cycle is shown in the upper part. Blue, red, and black are data of $\sqrt{P}$, $\alpha$, and leakage extracted by the CZ cycle.

**Table 2.** Error budget of single-qubit and CZ gates.

| Gate | $T$ (ns) | $p_{\mathrm{xeb}}$ | $r_{\mathrm{p,xeb}}$ | $p_{\mathrm{spb}}$ | $r_{\mathrm{p,spb}}$ | $r_{\mathrm{leak}}$ | $r_{\mathrm{p,dec}}$ | $r_{\mathrm{p,ctrl}}$ | Fidelity |
|---|---|---|---|---|---|---|---|---|---|
| Q1-$\pi/2$ | 50 | 99.78% | 0.16% | 99.82% | 0.13% | <0.01% | 0.12%–0.13% | 0.03% | 99.89% |
| Q2-$\pi/2$ | 50 | 99.80% | 0.15% | 99.81% | 0.14% | <0.01% | 0.13%–0.14% | 0.01% | 99.90% |
| Cycle-CZ | 156 | 98.84% | 1.09% | 98.99% | 0.95% | 0.22% | 0.73% | 0.14% | 99.13% |
| CZ | 106 | | 0.78% | | 0.68% | 0.20%–0.22% | 0.46%–0.48% | 0.10% | 99.38% |

For the numerical simulation without considering decoherence, the error of the CZ gate comes from leakage error, phase error, and swap error. The total error of these three parts can be suppressed to less than 0.01% with a duration of 100 ns easily. Limited by the fluctuation of the readout, we cannot sufficiently optimize the parameters of the control pulse, leading to the control error and leakage error (see Table 2) higher than numerical results. With the improvement of reading performance and system stability, it is hopeful of reducing the experiment error further.

In summary, we have demonstrated a fast and high-fidelity all-microwave CZ gate scheme on a new coupler structure design. The two-qubit gates can be realized fast thanks to this specific coupler design with stronger coupling strength. Meanwhile, all qubits are

decoupled except for applying two-qubit gates, facilitating parallel optimization on large-scale quantum devices in the future. Also, our CZ gate scheme is designed without any pulse correction, thus can be easily applied in real-time pulse generation.[2] Another essential advantage of our gate scheme is that it can be combined with frequency multiplexing technology. Microwave control pulses combined with on-chip filters[34,35] can be a feasible solution to reduce the number of control lines, as we can deliver the microwave of different frequencies through a common signal input to corresponding couplers through on-chip filters. Considering all these advantages above, our all-microwave CZ gate scheme can have broad application prospects in large-scale quantum hardware design in the future.

*Acknowledgments.* The authors thank the USTC Center for Micro- and Nanoscale Research and Fabrication for supporting the sample fabrication and QuantumCTek Co., Ltd. for supporting the fabrication and the maintenance of room-temperature electronics. This research was supported by the National Key R&D Program of China (Grant No. 2017YFA0304300), the Chinese Academy of Sciences, the Anhui Initiative in Quantum Information Technologies, the Technology Committee of Shanghai Municipality, the National Natural Science Foundation of China (Grants No. 11905217 and 11905294), the Natural Science Foundation of Shanghai (Grant No. 19ZR1462700), the Key-Area Research and Development Program of Guangdong Province (Grant No. 2020B0303030001), and the China Postdoctoral Science Foundation.

## References

[1] Campbell E T, Terhal B M, and Vuillot C 2017 *Nature* **549** 172
[2] Fowler A G, Mariantoni M, Martinis J M, and Cleland A N 2012 *Phys. Rev. A* **86** 032324
[3] Chen Z, Kelly J, Quintana C, Barends R, Campbell B, Chen Y, Chiaro B, Dunsworth A, Fowler A G, Lucero E, Jeffrey E, Megrant A, Mutus J, Neeley M, Neill C, O'Malley P J J, Roushan P, Sank D, Vainsencher A, Wenner J, White T C, Korotkov A N, and Martinis J M 2016 *Phys. Rev. Lett.* **116** 020501
[4] Barends R, Kelly J, Megrant A, Veitia A, Sank D, Jeffrey E, White T C, Mutus J, Fowler A G, Campbell B *et al.* 2014 *Nature* **508** 500
[5] Negirneac V, Ali H, Muthusubramanian N, Battistel F, Sagastizabal R, M, Marques S M, Marques J F, Vlothuizen W J, Beekman M *et al.* 2021 *Phys. Rev. Lett.* **126** 220502
[6] Li S, Castellano A D, Wang S, Wu Y, Gong M, Yan Z, Rong H, Deng H, Zha C, Guo C *et al.* 2019 *npj Quantum Inf.* **5** 1
[7] Sung Y, Ding L, Braumüller J, Vepsäläinen A, Kannan B, Kjaergaard M, Greene A, Samach G O, McNally C, Kim D *et al.* 2021 *Phys. Rev. X* **11** 021058
[8] Chen Y, Neill C, Roushan P, Leung N, Fang M, Barends R, Kelly J, Campbell B, Chen Z, Chiaro B *et al.* 2014 *Phys. Rev. Lett.* **113** 220502
[9] Li X, Cai T, Yan H, Wang Z, Pan X, Ma Y, Cai W, Han J, Hua Z, Han X *et al.* 2020 *Phys. Rev. Appl.* **14** 024070
[10] Collodo M C, Herrmann J, Lacroix N, Andersen C K, Remm A, Lazar S, Besse J C, Walter T, Wallraff A, and Eichler C 2020 *Phys. Rev. Lett.* **125** 240502
[11] Xu Y, Chu J, Yuan J, Qiu J, Zhou Y, Zhang L, Tan X, Yu Y, Liu S, Li J *et al.* 2020 *Phys. Rev. Lett.* **125** 240503
[12] Ye Y, Cao S, Wu Y, Chen X, Zhu Q, Li S, Chen F, Gong M, Zha C, Huang H L *et al.* 2021 *Chin. Phys. Lett.* **38** 100301
[13] McKay D C, Filipp S, Mezzacapo A, Magesan E, Chow J M, and Gambetta J M 2016 *Phys. Rev. Appl.* **6** 064007
[14] Sete E A, Didier N, Chen A Q, Kulshreshtha S, Manenti R, and Poletto S 2021 *Phys. Rev. Appl.* **16** 024050
[15] Kosen S, Li H X, Rommel M, Shiri D, Warren C, Grönberg L, Salonen J, Abad T, Biznárová J, Caputo M *et al.* 2021 arXiv:2112.02717 [quant-ph]
[16] Ganzhorn M, Salis G, Egger D, Fuhrer A, Mergenthaler M, Müller C, Müller P, Paredes S, Pechal M, Werninghaus M *et al.* 2020 *Phys. Rev. Res.* **2** 033447
[17] Sheldon S, Magesan E, Chow J M, and Gambetta J M 2016 *Phys. Rev. A* **93** 060302
[18] Kandala A, Wei K, Srinivasan S, Magesan E, Carnevale S, Keefe G, Klaus D, Dial O, and McKay D 2021 *Phys. Rev. Lett.* **127** 130501
[19] Barends R, Quintana C, Petukhov A, Chen Y, Kafri D, Kechedzhi K, Collins R, Naaman O, Boixo S, Arute F *et al.* 2019 *Phys. Rev. Lett.* **123** 210501
[20] Foxen B, Mutus J, Lucero E, Jeffrey E, Sank D, Barends R, Arya K, Burkett B, Chen Y, Chen Z *et al.* 2019 *Supercond. Sci. Technol.* **32** 015012
[21] Rol M A, Ciorciaro L, Malinowski F K, Tarasinski B M, Sagastizabal R E, Bultink C C, Salathe Y, Haandbæk N, Sedivy J, and DiCarlo L 2020 *Appl. Phys. Lett.* **116** 054001
[22] Andersen C K, Remm A, Lazar S, Krinner S, Heinsoo J, Besse J C, Gabureac M, Wallraff A, and Eichler C 2019 *npj Quantum Inf.* **5** 69
[23] Nelder J A and Mead R 1965 *Comput. J.* **7** 308
[24] McKinnon K I 1998 *SIAM J. Optim.* **9** 148
[25] Rol M, Bultink C C, O'Brien T E, De Jong S, Theis L S, Fu X, Luthi F, Vermeulen R F, De Sterke J, Bruno A *et al.* 2017 *Phys. Rev. Appl.* **7** 041001
[26] Sendelbach S, Hover D, Mück M, and McDermott R 2009 *Phys. Rev. Lett.* **103** 117001
[27] Fried E S, Sivarajah P, Didier N, Sete E A, da S M P, Johnson B R, and Ryan C A 2019 arXiv:1908.11370 [quant-ph]
[28] Megrant A, Neill C, Barends R, Chiaro B, Chen Y, Feigl L, Kelly J, Lucero E, Mariantoni M, O'Malley P J *et al.* 2012 *Appl. Phys. Lett.* **100** 113510
[29] Knill E, Leibfried D, Reichle R, Britton J, Blakestad R B, Jost J D, Langer C, Ozeri R, Seidelin S, and Wineland D J 2008 *Phys. Rev. A* **77** 012307
[30] Epstein J M, Cross A W, Magesan E, and Gambetta J M 2014 *Phys. Rev. A* **89** 062321
[31] Proctor T, Rudinger K, Young K, Sarovar M, and Blume-Kohout R 2017 *Phys. Rev. Lett.* **119** 130502
[32] Boixo S, Isakov S V, Smelyanskiy V N, Babbush R, Ding N, Jiang Z, Bremner M J, Martinis J M, and Neven H 2018 *Nat. Phys.* **14** 595
[33] Arute F, Arya K, Babbush R, Bacon D, Bardin J C, Barends R, Biswas R, Boixo S, Brandao F G, Buell D A *et al.* 2019 *Nature* **574** 505
[34] Dai D and Bowers J E 2014 *Nanophotonics* **3** 283
[35] Kobe O B, Chuma J, Jamisola J R, and Chose M 2017 *Eng. Sci. Technol. Int. J.* **20** 460

# Supplementary information of "Realization of fast all-microwave CZ gates with a tunable coupler"

Shaowei Li,[1,2,3] Daojin Fan,[1,2,3] Ming Gong,[1,2,3] Yangsen Ye,[1,2,3] Xiawei Chen,[1,2,3] Yulin Wu,[1,2,3] Huijie Guan,[1,2,3] Hui Deng,[1,2,3] Hao Rong,[1,2,3] He-Liang Huang,[1,2,3] Chen Zha,[1,2,3] Kai Yan,[1,2,3] Shaojun Guo,[1,2,3] Haoran Qian,[1,2,3] Haibin Zhang,[1,2,3] Fusheng Chen,[1,2,3] Qingling Zhu,[1,2,3] Youwei Zhao,[1,2,3] Shiyu Wang,[1,2,3] Chong Ying,[1,2,3] Sirui Cao,[1,2,3] Jiale Yu,[1,2,3] Futian Liang,[1,2,3] Yu Xu,[1,2,3] Jin Lin,[1,2,3] Cheng Guo,[1,2,3] Lihua Sun,[1,2,3] Na Li,[1,2,3] Lianchen Han,[1,2,3] Cheng-Zhi Peng,[1,2,3] Xiaobo Zhu,[1,2,3,*] and Jian-Wei Pan[1,2,3]

[1]*Department of Modern Physics, University of Science and Technology of China, Hefei 230026, China*

[2]*Shanghai Branch, CAS Center for Excellence in Quantum Information and Quantum Physics, University of Science and Technology of China, Shanghai 201315, China*

[3]*Shanghai Research Center for Quantum Sciences, Shanghai 201315, China*

(Dated: January 30, 2022)

* xbzhu16@ustc.edu.cn

## I. NUMERICAL SIMULATION OF CZ GATE

We designed three different couplers and compared the quality of different designs according to the CZ error achieved under different qubit detune frequency $\Delta = \omega_{10} - \omega_{01}$. We first set $g = 0$ for three types of the coupler, labeled as Con. 1, Con. 2, and Con. 3. We set different g for idle working points to find the effect of idle point setting, labeled as Con. 3, Con. 4, and Con. 5. Also, we test the influence of envelopes of the microwave by comparing two types of envelopes labeled as Con. 3, and Con. 6. Fig.S1 shows 6 condition for numerical simulation. Fig.S2 shows the different CZ error results between coupler design 1 and coupler design 3. Fig.S3 shows the different CZ error results between coupler design 2 and coupler design 3. Fig.S4 shows the results of different coupling strength setting for idle points. Fig.S5 shows the results of different initial envelope settings for idle points.

For each $\Delta/2\pi$ in Fig. 4(d) in main text, we set the initial ratio of $\vec{\lambda}$ as $\lambda_1 : \lambda_2 : \lambda_3 : \lambda_4 = -0.0760 : 1.0000 : 0.4222 : -0.1636$, and chose static frequency difference between $|11\rangle$ and $|20\rangle$ as the initial microwave frequency. Also, the averaging microwave amplitude $\bar{A}(t)$ was set to be 0.4, 0.045 or 0.05. Then we used the Nelder Mead algorithm to optimize the fidelity of the CZ gate. Fig.S6 and Fig.S7 show the numerical optimization and time domain evolution at $\Delta/2\pi = 0.11724$ GHz, where no unwanted interaction is activated and CZ gate with 99.99972% fidelity is achieved. Fig.S8 and Fig.S9 show the numerical optimization and time domain evolution at $\Delta/2\pi = 0.09248$ GHz, where no unwanted interaction is activated and CZ gate with 99.99960% fidelity is achieved. Fig.S10 and Fig.S11 show the numerical optimization and time domain evolution at $\Delta/2\pi = 0.10486$ GHz, where the interaction between $|01\rangle$ and $|01\rangle$ is activated and the optimized CZ fidelity is 99.75%. Fig.S12 and Fig.S13 show the numerical optimization and time domain evolution at $\Delta/2\pi = 0.07391$ GHz, where the interaction between $|11\rangle$ and $|02\rangle$ activated and the optimized CZ fidelity is 99.39%.

## II. EXPERIMENT OF CZ GATE

The definition of cross entropy benchmarking (XEB) is as below,

$$\alpha = \frac{\overline{\sum_q p_m(q)(Dp_s(q) - 1)}}{D\sum_q \overline{p_s(q)^2} - 1} \tag{S1}$$

with $\alpha$ as the sequence fidelity, $D = 2^N$, $N$ is the number of qubits, $q$ is the sampled qubit state bitstrings (for single-qubit XEB, $q$ is 0 or 1), $p_s(q)$ is the ideal probability of $q$, and $p_m(q)$ is the measured probability of $q$. The over lines in Eq. S1 refer to the average of the random circuits in each cycle. Meanwhile, we use the speckle purity benchmarking (SPB) to measure the effect of decoherence error. Here,

$$\sqrt{P} = \sqrt{Var(p_m)\frac{D^2(D+1)}{D-1}}. \tag{S2}$$

and $Var(P_m)$ the variance of the experimental probabilities extracted from the XEB experiment.

Due to the readout error, the start points (m = 0) of $\alpha$ are not at 1 in Fig.4(c) and (d). The setting of readout pulse in our experiment was different for $|0\rangle$, $|1\rangle$ measurement and for $|0\rangle$, $|1\rangle$, $|2\rangle$ measurement. For $|0\rangle$, $|1\rangle$ measurement, the matrixes of readout fidelity are labeled as below,

$$\begin{pmatrix} F_{00} & F_{01} \\ F_{10} & F_{11} \end{pmatrix}_{Q1} = \begin{pmatrix} 0.9551 & 0.0449 \\ 0.1581 & 0.8419 \end{pmatrix} \tag{S3}$$

and

$$\begin{pmatrix} F_{00} & F_{01} \\ F_{10} & F_{11} \end{pmatrix}_{Q2} = \begin{pmatrix} 0.9475 & 0.0525 \\ 0.1517 & 0.8483 \end{pmatrix}. \tag{S4}$$

For $|0\rangle$, $|1\rangle$, $|2\rangle$ measurement, the matrixes of readout fidelity are labeled as below,

$$\begin{pmatrix} F_{00} & F_{01} & F_{02} \\ F_{10} & F_{11} & F_{12} \\ F_{20} & F_{21} & F_{22} \end{pmatrix}_{Q1} = \begin{pmatrix} 0.9050 & 0.0632 & 0.0318 \\ 0.1633 & 0.7779 & 0.0588 \\ 0.1383 & 0.2005 & 0.6612 \end{pmatrix} \tag{S5}$$

and

$$\begin{pmatrix} F_{00} & F_{01} & F_{02} \\ F_{10} & F_{11} & F_{12} \\ F_{20} & F_{21} & F_{22} \end{pmatrix}_{Q2} = \begin{pmatrix} 0.8767 & 0.0534 & 0.0699 \\ 0.1887 & 0.7399 & 0.0714 \\ 0.1645 & 0.1784 & 0.6571 \end{pmatrix}. \tag{S6}$$

Here $F_{ij}$ represents the probability of measuring $|j\rangle$ when we prepared the initial state of $|i\rangle$. In experiment, we used the product of each matrix of single-qubit readout fidelity as the matrix of multi-qubit readout fidelity. In Fig.4(c) and (d), the $\alpha$ and $\sqrt{P}$ are calculated by the raw probability of $|0\rangle$, $|1\rangle$ measurement, and the $leak$ is the probability corrected according to the matrix of multi-qubit readout fidelity of $|0\rangle$, $|1\rangle$, $|2\rangle$ measurement. Here, $leak = P_{|02\rangle} + P_{|12\rangle} + P_{|20\rangle} + P_{|21\rangle} + P_{|22\rangle}$.

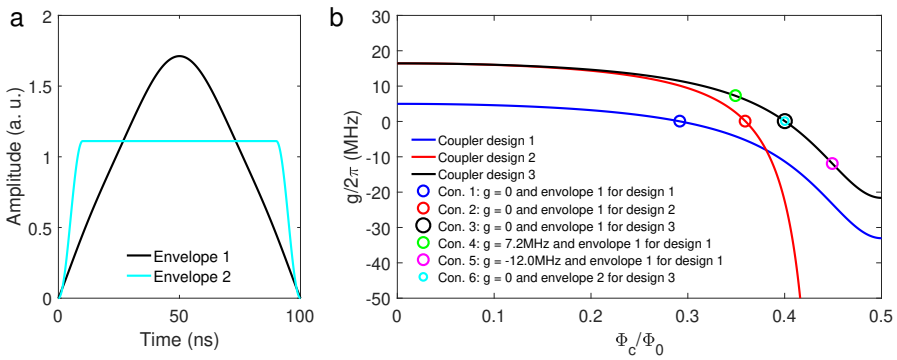


FIG. S1. Different coupler designs, idle points and initial envelopes for condition 1 (con. 1) to condition 6.

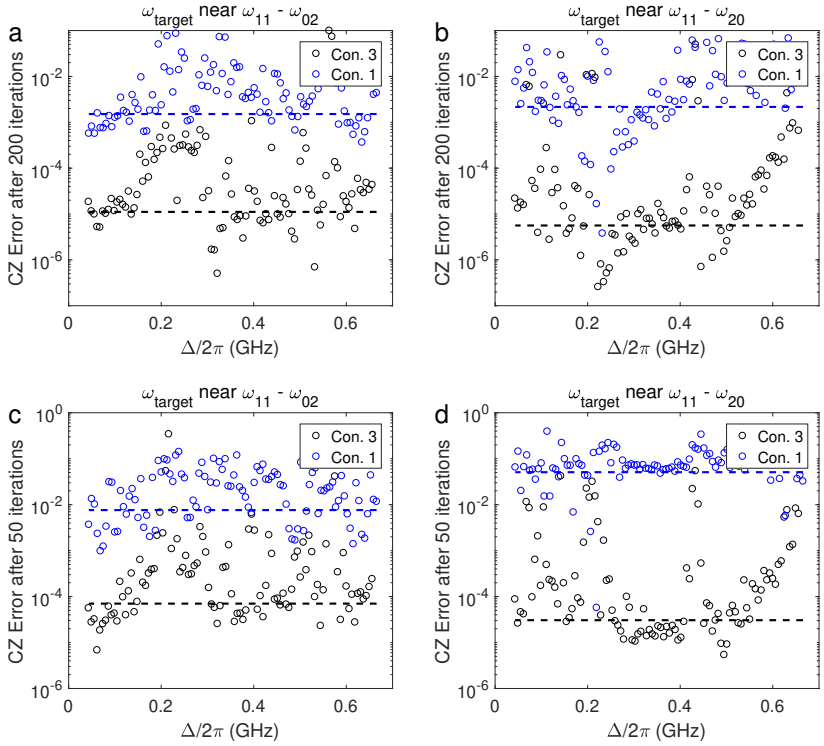


FIG. S2. Results of Con. 3 and Con. 1 of CZ optimization. (a) CZ error under the con. 1 and con. 3 for selecting $\omega_{target}$ near $\omega_{11} - \omega_{02}$. The circles are CZ errors under con. 3 and con. 1 after 200 iteration of Nelder Mead algorithm for different $\Delta$. For some of $\Delta$, the unnecessary resonance interactions will increase the gate error, see Fig. 2 (d) in main text. We selected the best 50 from the results of all 100 different $\Delta$ to calculate the average error rate, as shown by the dash line. (b) CZ error under the con. 1 and con. 3 for selecting $\omega_{target}$ near $\omega_{11} - \omega_{20}$ after 200 iteration. (c) CZ error under the con. 1 and con. 3 for selecting $\omega_{target}$ near $\omega_{11} - \omega_{02}$ after 50 iteration. (d) CZ error under the con. 1 and con. 3 for selecting $\omega_{target}$ near $\omega_{11} - \omega_{20}$ after 50 iteration.

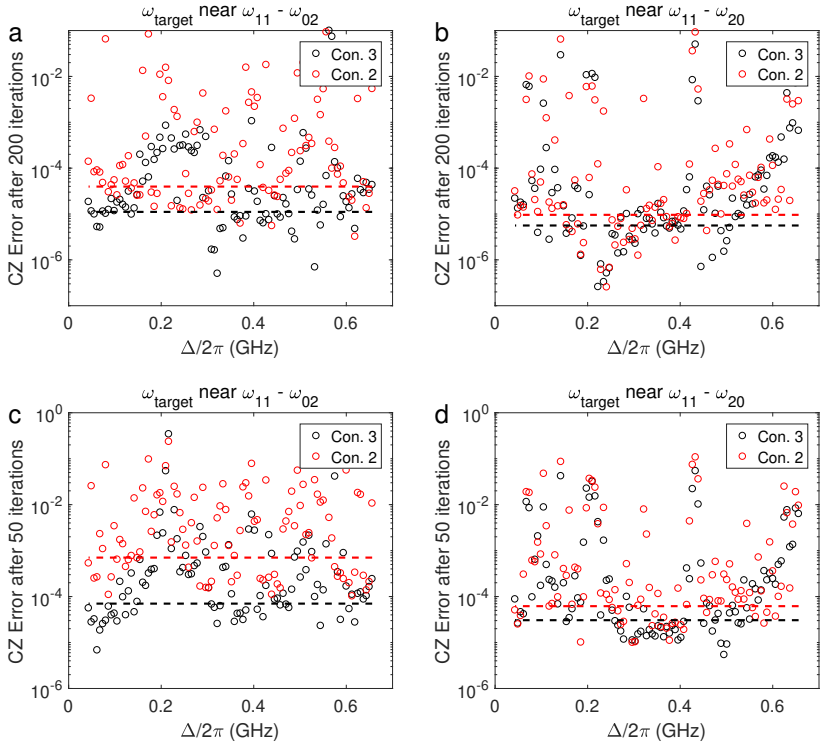


FIG. S3. Results of Con. 3 and Con. 2 of CZ optimization.

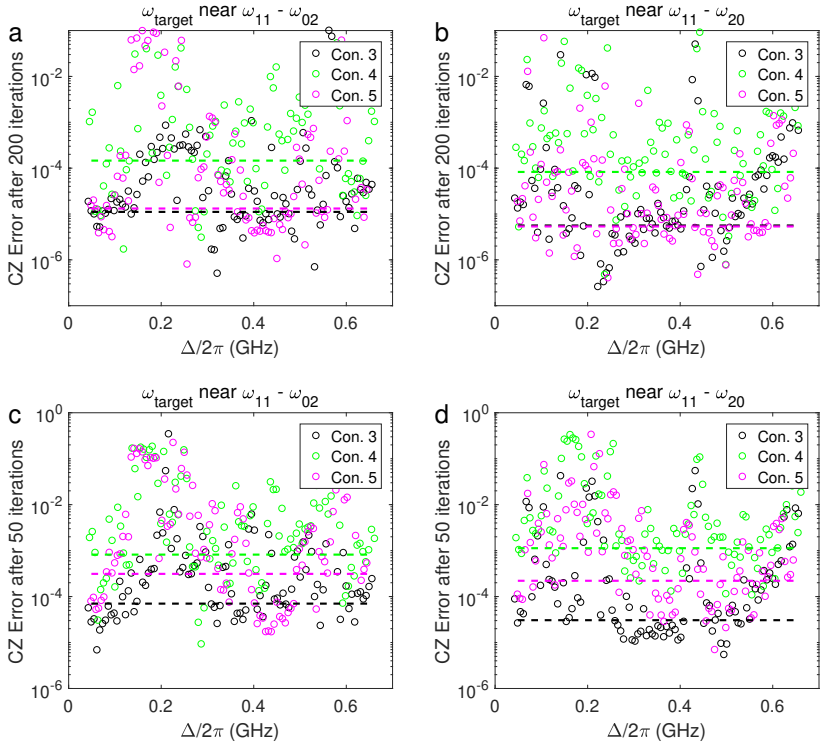


FIG. S4. Results of Con. 3, Con. 4 and Con. 5 of CZ optimization.

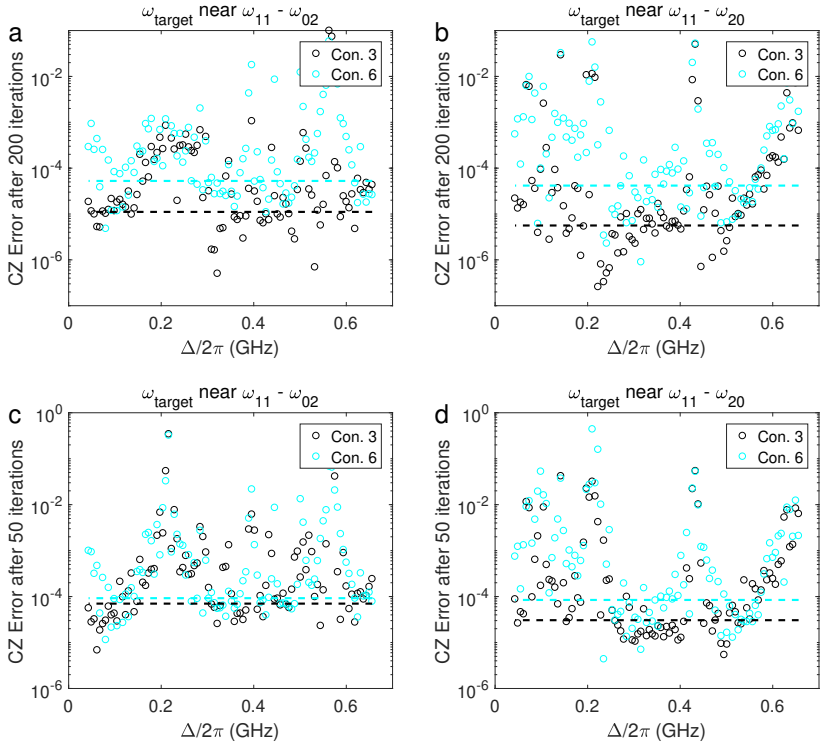


FIG. S5. Results of Con. 3 and Con. 6 of CZ optimization.

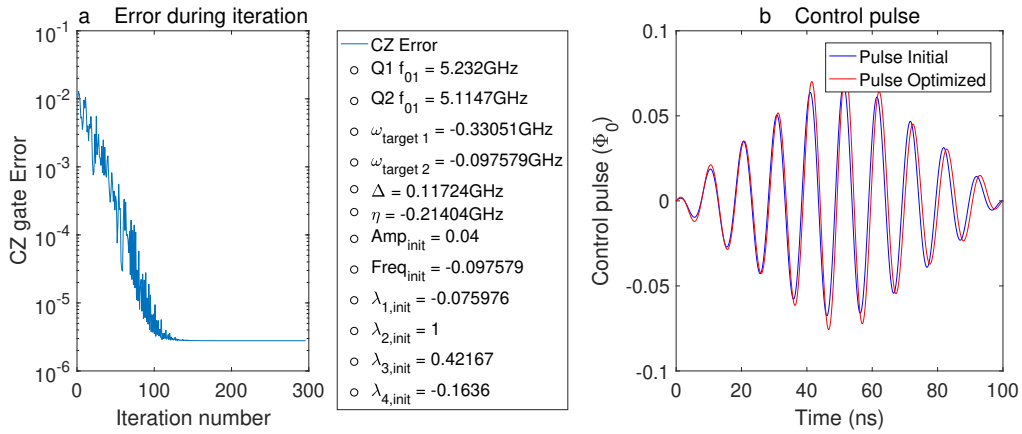


FIG. S6. Numerical optimization at $\Delta/2\pi = 0.11724$ GHz in Fig. 2(d) in main text. (a) shows the qubits work point, initial value of CZ pulse and CZ gate error during iteration. (b) shows the control pulse before and after optimization.

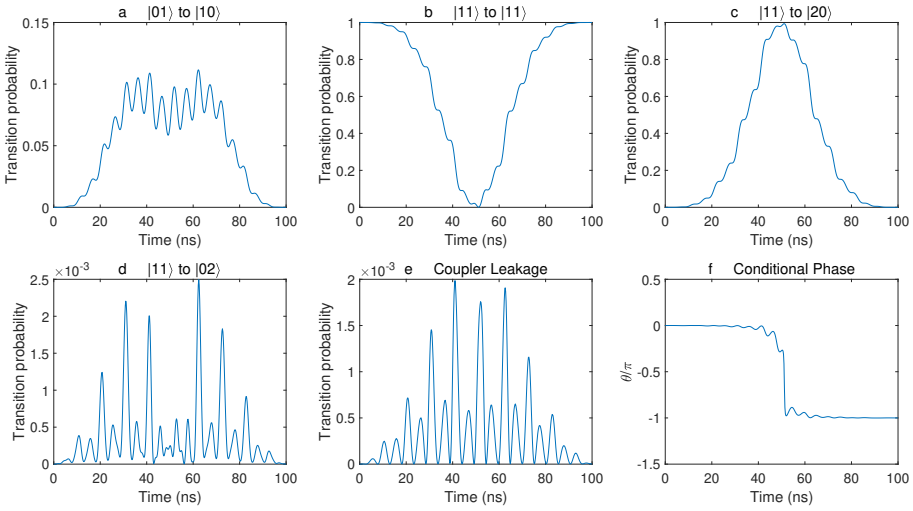


FIG. S7. Time domain quantum evolution for optimized CZ pulse at $\Delta/2\pi = 0.11724$ GHz (data obtained by numerical simulation method). The quantum state in this figure is the energy eigenstate of the static Hamiltonian. (a) (d) show the transtion probability between different quantum states. (e) shows the probability of leakage into the excited state of the coupler. (f) shows the conditional phase during the evolution.

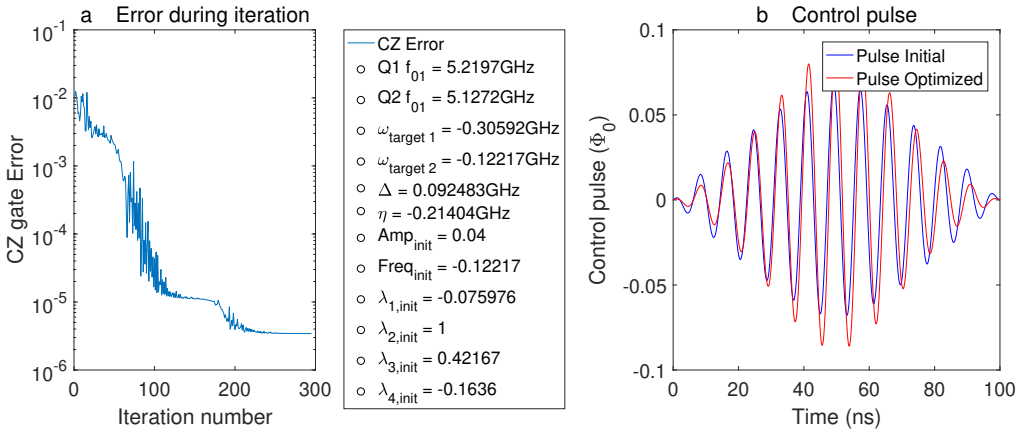


FIG. S8. Numerical optimization at $\Delta/2\pi = 0.09248$ GHz in Fig. 2(d) in main text.

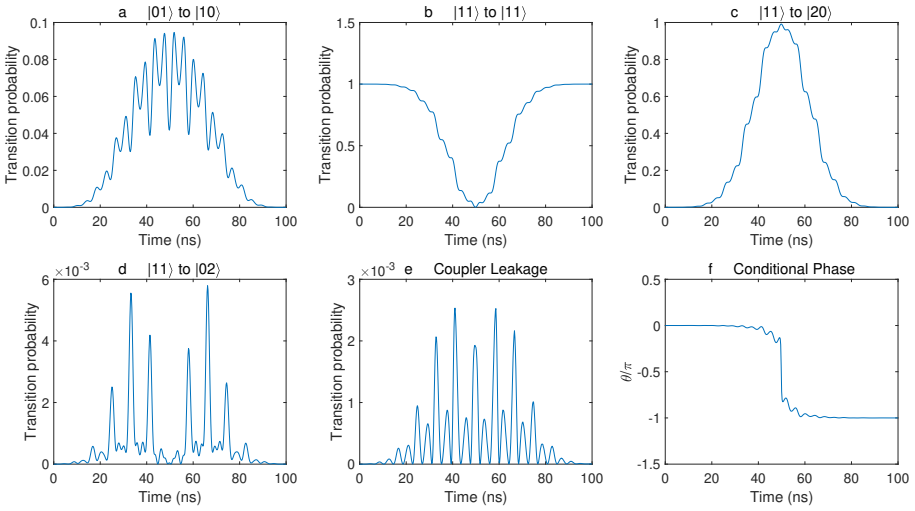


FIG. S9. Time domain quantum evolution for optimized CZ pulse at $\Delta/2\pi = 0.09248$ GHz.

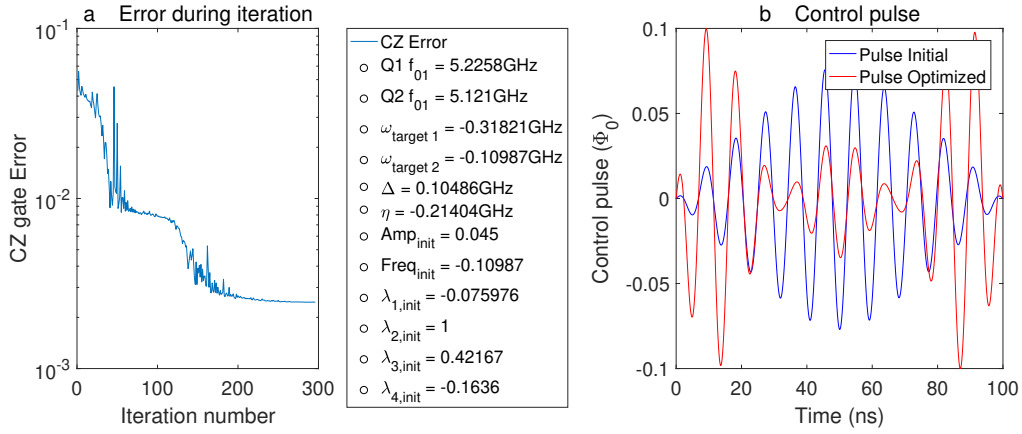


FIG. S10. Numerical optimization at $\Delta/2\pi = 0.10486$ GHz in Fig. 2(d) in main text. For this $\Delta$, the interaction between $|01\rangle$ and $|10\rangle$ is activated.

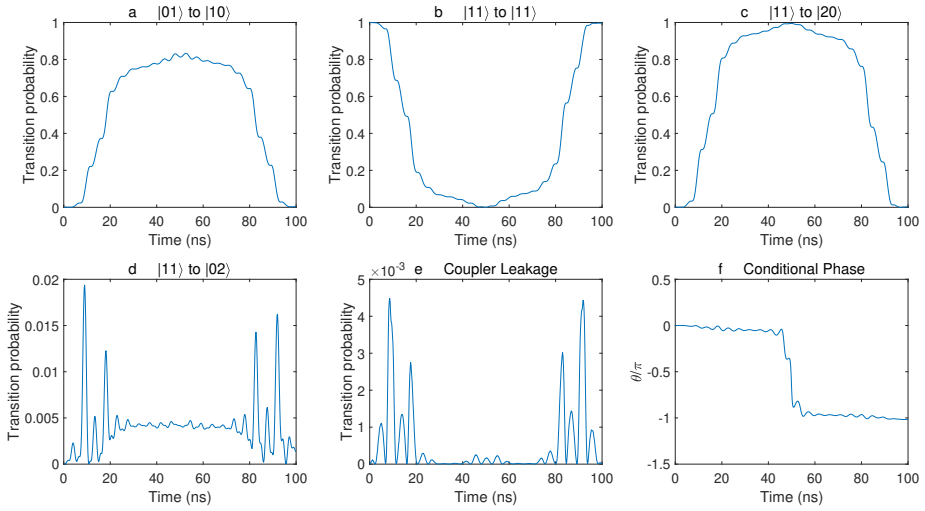


FIG. S11. Time domain quantum evolution for optimized CZ pulse at $\Delta/2\pi = 0.10486$ GHz.

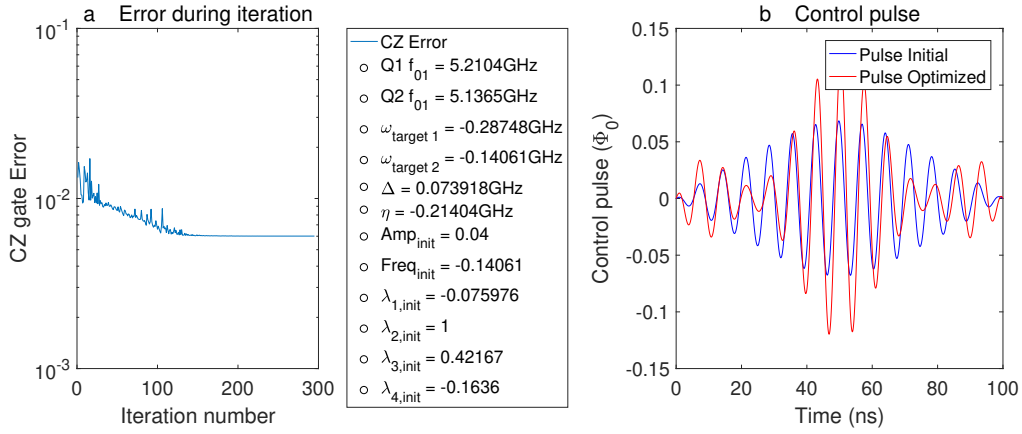


FIG. S12. Numerical optimization at $\Delta/2\pi = 0.07392$ GHz in Fig. 2(d) in main text. For this $\Delta$, the interaction between $|11\rangle$ and $|02\rangle$ is activated.

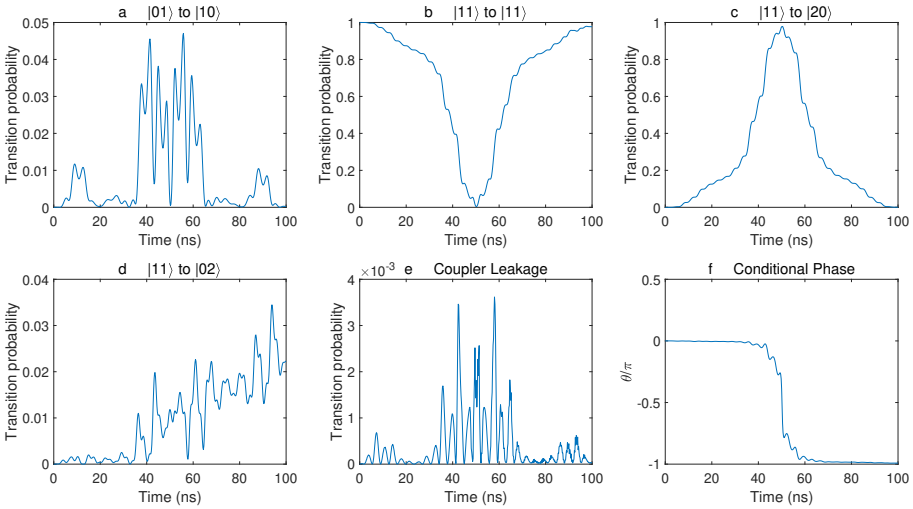


FIG. S13. Time domain quantum evolution for optimized CZ pulse at $\Delta/2\pi = 0.07392$ GHz.